ZnO Nanoparticles Anchored To Silica Filler. A Curing Accelerator for Isoprene Rubber Composites

A. Susanna,[a] L. Armelao,[b] E. Callone,[c] S. Dirè,[c] M. D'Arienzo,[a] B. Di Credico,[a] L. Giannini,[d] T. Hanel,[d] F. Morazzoni,[a] R. Scotti[a*]

[a] *Dept. of Scienza dei Materiali, INSTM, University of Milano-Bicocca, Via R. Cozzi, 55, 20125 Milano, Italy. Fax: +39-02-64485400; Tel: +39-02-64485133; E-mail:roberto.scotti@unimib.it;*

[b] *IENI – CNR and INSTM, Dept. of Chemical Sciences, University of Padova, Via F. Marzolo, 1, 35131 Padova, Italy;*

[c] *Dept. of Ingegneria Industriale, University of Trento, Via Sommarive, 9, 38123 Trento, Italy;*

[d] *Pirelli Tyre SpA, Viale Sarca, 222, 20126 Milano Italy.*

KEYWORDS: rubber nanocomposite, zinc oxide, silica filler, sol-gel, curing accelerator, vulcanization, sol-gel.

ABSTRACT

ZnO nanoparticles (NPs) were anchored to SiO_2 spherical nanoparticles by hydrolysis and condensation of $Zn(CH_3COO)_2$ in the presence of SiO_2. The ZnO/SiO_2 composite was then blended with isoprene rubber. The immobilization of ZnO NPs on the silica surface, due to covalent Si-O-Zn bonds provides a homogeneous dispersion of zinc in the rubber matrix and increases the accessibility of the curative reactants to Zn^{2+} ions. This improves the efficiency of the rubber curing and reduces the amount of used ZnO.

1. Introduction

Sulfur vulcanization is a consolidated process of the tire industry to improve the mechanical properties of unsaturated rubber (*e.g.* elasticity, tensile strength, abrasion) by a crosslinked polymeric network [1,2]. The crosslinks are predominantly from mono-, bi- and polysulphides; their amount depends on the vulcanization procedure i.e. the curing chemicals added to rubber [3].

In general it is desirable to enhance the vulcanization rate in order to decrease time and energy [4,3,5]. Over the years different additives acting as accelerators [6] or activators [7,8] have been employed. Representative accelerators of the curing rate are organics like thiazoles and sulphenamides [4], in many case assisted by secondary accelerators like thiourams and dithiocarbamates [9]. They interact with the molecular sulfur via radicalic or ionic pathways forming polysulfidic cross-linking moieties able to bind the rubber chains [3]. Activators are instead inorganic metal derivatives (*e.g.* ZnO, MgO, $Ca(OH)_2$), able to form adducts with accelerators and to further increase their efficiency [7]. Among the activators, ZnO is considered the most efficient, and it is currently used in the industrial curing procedures. The inorganic activators are often used in association with fatty acids, like stearic acid, which favour their dissolution into the rubber [10]. In spite of the established curing procedures, the role of activators and accelerators and the nature of the active sulphurating agents are not yet fully understood because of the complex mechanism of the process [4]. Several studies have suggested that Zn^{2+} ions, generated by interaction of ZnO with stearic acid, give rise to organometallic complexes with the accelerator molecules and sulfur, which are more efficient sulphurating agents than the free accelerators [11]. The capability of Zn^{2+} ions in forming complexes is the key point of the activation mechanism and strongly depends on the ZnO dispersion in the polymer matrix and on the crystal structure of the metal oxide. In fact, crystalline nanoparticles (NPs) do not easily disperse in the rubber matrix, and only a relatively small amount of the ZnO actually reacts with the other curing compounds.

Microsized ZnO crystal particles are commonly employed in curing processes. Unfortunately, the oxide undergoes leaching during the production, disposal and recycling of rubber and under tire operative conditions, leading to an excess of the metal in the environment with potentially negative effects [12]. Thus, over the last few years the reduction of ZnO level in rubber curing has become a very urgent issue [13].

Different approaches have been proposed to face this challenge [14,15]. Among them the use of ZnO NPs has recently received a great deal of interest because of the better dispersion in rubber and the increased curing efficacy due to their high surface-to-volume ratio [16-18].

Many different methods (*e.g.* solvothermal, hot-injection, miniemulsion) have been proposed to obtain ZnO NPs [19]. Although the morphological control is really good, these techniques are not cost-effective and only sub-gram quantities can be obtained. Moreover, the large-scale synthesis of ZnO in the form of homogeneous and well dispersed spherical NPs is difficult, due to the tendency of this oxide to crystallize in hexagonal phase, growing along selective crystal planes and giving anisotropic crystals [20]. A promising approach to achieve this goal consists in the growth of ZnO directly on the surface of supporting oxides, in order to maximize the ZnO-support interaction, minimizing that among the ZnO particles and thus controlling the particle size [21,22].

In this context, the present work proposes the anchoring of silica particles with ZnO NPs [23]. This allows to utilize ZnO/SiO_2 NPs as curing activator and simultaneously reinforcing filler, decreasing the zinc amount in rubber composites.

Moving from the literature methods for obtaining ZnO/SiO_2 NPs, a simple low temperature sol-gel route [24] was employed, based on the hydrolysis of zinc acetate in NaOH ethanol solution and condensation in the presence of silica particles. Synthesis parameters (zinc loading, base concentration) were varied to obtain:

- homogeneously sized (4-6 nm diameter) and spherical shaped ZnO NPs, dispersed on the surface of silica particles, which maximize the accessibility of Zn^{2+} ions;
- ZnO particles immobilized by strong chemical bonds to minimize the potential release of the oxide from silica.

The morphology and the crystal structure of ZnO/SiO_2 NPs were investigated by X-Ray Diffraction (XRD) and Transmission Electron Microscopy (TEM). The nanometric size was also assessed by UV reflectance measurements. The Si-O-Zn bond interaction was comprehensively studied by Solid State Nuclear Magnetic Resonance (NMR), Attenuated Total Reflection- Fourier Transform Infrared Spectroscopy (ATR-FTIR) and X-ray Photoelectron Spectroscopy (XPS), and it was discussed in relation to the NP dimensions.

ZnO anchored silica NPs were used by ex-situ blending to prepare cured poliisoprene (IR) nanocomposites loaded with 40 phr (parts per hundred rubber) of silica.

Finally, curing efficiency and dynamic mechanical properties of vulcanized ZnO/SiO_2 nanocomposites were investigated and compared to those obtained by using powdered crystalline ZnO as activator in conventional curing processes.

2. Experimental

2.1. Materials

SiO_2/ZnO synthesis: precipitated silica Rhodia Zeosil MP1165 (BET specific surface area 160 $m^2\ g^{-1}$); $Zn(CH3COO)_2{\cdot}2H_2O$ (99.99 %) from Carlo Erba; NaOH (98 %) from Fluka; anhydrous ethanol EtOH (99.9%) from Scharlau used as solvent; Milli-Q water with resistivity > 18.2 MΩ•cm.

Compounding: Cis-1,4-polyisoprene rubber (IR), from Nizhnekamskneftechim Expor; bis(3-triethoxysilylpropyl) disulfide, TESPD, from Aldrich; antioxidant N-(1,3-dimethylbutyl)-N'-phenyl-p-phenylenediamine, 6PPD Santoflex-6PPD from Flexsys; stearic acid Stearina TP8 from Undesa; N-

cyclohexyl-2-benzothiazole sulfenamide, CBS, Vulkacit CZ/C from Lanxess; sulphur Creso from Redball Superfine; ZnO from Zincol Ossidi (wurtzite, BET specific surface area 5 $m^2 g^{-1}$).

2.2 Synthesis of ZnO anchored SiO_2 nanoparticles

ZnO/SiO_2 NPs were prepared by sol-gel procedure. SiO_2 powders (0.426 mol) were dispersed in 0.9 l of ethanol by sonication for 10 min (pulses: 1s; 20 kHz). Then suitable amounts of $Zn(CH_3COO)_2\ 2H_2O$ and NaOH (Table 1) were added under stirring to the SiO_2 suspension at 65 °C. ZnO NPs formed by hydrolysis and condensation on the silica surface (see later). Samples with different amounts of zinc precursor (0.96-0.035 Zn/Si molar ratio) (Table1) were prepared. After 20 minutes ZnO/SiO_2 particles were filtered, successively washed four times with ethanol and dried in air at room temperature. In the absence of silica a stable colloidal solution formed, and no precipitation of ZnO NPs occurred.

The actual loading of ZnO was evaluated by Inductively Coupled Plasma-Atomic Emission Spectroscopy (ICP-AES) (see later) and resulted lower than the nominal one (Table 1).

Table 1: Synthesis reactants and ZnO content of ZSO-X

Name	$Zn(CH_3COO)_2 \cdot 2H_2O$ (mol)	SiO_2 (mol)	ZnO (wt%)
ZSO-50.2	0.409	0.426	50.2
ZSO-14.2	0.205	0.426	14.2
ZSO -7.7	0.081	0.426	7.7
ZSO -4.0	0.015	0.426	4.0

The sol-gel reaction yield ranged between 50 to 90 % and depended on the basicity of the solution. In fact, by maintaining the same amount of zinc precursor, the ZnO loading increases with the amount of hydroxide, and in the absence of hydroxide no ZnO grew on silica particles.

Hereafter, ZnO anchored to SiO_2 NPs will be labelled ZSO-X, where X refers to the actual amount (weight %) of ZnO on SiO_2.

2.3. Characterization of ZnO anchored SiO_2 NPs

The amount of ZnO in ZSO-X was measured with ICP-AES with a ICP-OES Optima 7000 DV Perkin Elmer instrument. Specimens for the analysis were prepared by thinly grinding 0.2 g of powdered samples and dissolving them in a Teflon beaker with 5 mL of HF 49%. Then the solution was dried and the residue rinsed five times with 3 mL of HCl 37%. Finally, the obtained solution was dried again, and the solid dissolved with MQ water and diluted in a 250 mL calibrated flask. Before analysis a further dilution 1:100 was carried out.

The presence of crystalline phases was assessed by conventional XRD using a Bruker D8 Advance instrument, having a Cu Kα incident beam (λ = 1.5406 Å). The morphological characterization of ZSO-X powders was performed on a Jeol 3010 High Resolution Transmission Electron Microscope operating at 300 kV with a high-resolution pole piece (0.17 nm point to point resolution) and equipped with a Gatan slow-scan 794 CCD camera. The powders were suspended in isopropanol, and a 5 µL drop of this suspension was deposited on a holey carbon film supported on 3 mm copper grid for TEM investigation.

Reflectance UV-Vis analysis (range 400-200 nm) was performed by a UV Lambda 900 Perkin Elmer spectrometer on powdered samples to determine the absorption edge energy of ZnO. The absorption onset can be obtained by plotting $\ln^2(I_t/I_0)$ vs. energy [25].

Solid state NMR analyses were carried out with a Bruker 400WB spectrometer operating at a proton frequency of 400.13 MHz. Magic-Angle Spinning-NMR (MAS NMR) spectra were acquired with single pulse (SP) experiments and cross polarization (CP) pulse sequences under the following conditions. CP: ^{29}Si frequency: 79.48 MHz, $\pi/2$ pulse 3.9 µs, decoupling length 6.3 µs, recycle delay: 10 s, 5k scans. SP: $\pi/4$ pulse 3.9 µs, recycle delay 100 s, 2k scans. Samples were packed in 4 mm zirconia rotors, which were spun at 6 kHz under air flow. Adamantane, Q8M8 and EtOH were used as external secondary references. Si units were labelled according to the usual NMR notation, Q_n representing a tetrafunctional Si unit within bridging O atoms.

ATR-FTIR analysis was performed by a Perkin Elmer Spectrum 100 instrument (1 cm^{-1} resolution spectra, 650-4000 cm^{-1} region, 16 scans).

XPS was used to assess the surface composition of the ZSO-X samples. Spectra were obtained by a Perkin-Elmer *Φ* 5600-ci spectrometer using non-monochromatized Al Kα radiation (1486.6 eV). Samples were mounted on steel holders and introduced directly into the fast-entry lock system of the XPS analytical chamber. The analysis area was 800 μm in diameter and the working pressure was lower than 10-9 mbar. The spectrometer was calibrated by assuming the binding energy (BE) of the Au 4f7/2 line at 83.9 eV with respect to the Fermi level. The standard deviation for the BEs values was ± 0.2 eV. Survey scans were obtained in the 0−1300 eV range. Detailed scans were recorded for the C1s, O1s, Na1s, Si2p and Zn2p regions. No further element was detected. Charging effects were corrected by assigning to the C1s peak associated with adventitious hydrocarbons a value of 284.8 eV [26]. The analysis involved Shirley-type background subtraction [27] non-linear least-squares curve fitting adopting Gaussian-Lorentzian peak shapes, and peak area determination by integration. The atomic compositions were evaluated from peak areas using sensitivity factors supplied by Perkin-Elmer, taking into account the geometric configuration of the apparatus. The experimental uncertainty on the reported atomic composition values did not exceed ± 5%.

2.4. Preparation of silica/IR nanocomposites

Uncured nanocomposite materials were prepared by mixing IR with a filler mixture of SiO_2 Zeosil MP1165 and ZSO-4.0, corresponding to a total amount of 40 phr SiO_2, in a Thermo Haake Reomix lab station internal mixer (250 mL mixing chamber, 0.7 filling factor), working at temperature of 120 °C. Composites with different ZnO content were prepared (1.6, 1.2, 0.60, 0.05 phr) by varying the SiO_2:ZSO ratio. Coupling agent TESPD (1.2 phr) and antioxidant 6PDD (0.62 phr) were also mixed. Sheets of about 2 mm thickness were obtained by 2 min mixing in an open two-roll mill. Nanocomposites were cured according to the following procedure. Firstly, stearic acid (0.62 phr) was added to the composite

over 2 min and then the sample was mixed for 4 min. at 60 rpm with dumping at 140 °C. Successively, the other vulcanization reactants, i.e. S8 (0.9 phr) and CBS (0.48 phr), were added by mixing at 90 °C for 3 min in a two-roll mill. Composites were further molded for 2 min to produce sheets of about 2 cm thick, suitable for the vulcanization. Curing profiles were measured with a Moving Die Rheometer (RPA 2000, Alpha Technological) under the following conditions: ± 1° oscillation angle, 170 °C temperature, 4.3 bar pressure and 30 min running time. This analysis gave the optimum conditions for the curing. Hereafter, the cured samples will be called YZSO-IR, where Y indicates the ZnO content expressed in phr. Reference master batches were also prepared following the same conditions reported for YZSO-IR by mixing IR with 40 phr of SiO_2 Zeosil MP1165 (Table 2). In this case, crystalline ZnO powder was conventionally added in the first step of vulcanization chemical mixing. Cured reference samples will be labelled as M-YZSO-IR, where Y indicates the ZnO content expressed in phr. The amounts of filler and ZnO utilized in the vulcanization procedure are reported in Table 2.

Table 2: Filler and ZnO loading of YZSO-IR and M-YZSO-IR nanocomposites (in phr)

Samples	**IR**	**SiO_2**	**ZSO-4.0**	**ZnO**
1.6 ZSO-IR	100	1.6	40.0	-
1.2 ZSO-IR	100	11.2	30.0	-
0.60 ZSO-IR	100	25.6	15.0	-
0.25 ZSO-IR	100	34.0	6.30	-
0.05 ZSO-IR	100	38.8	1.25	-
M-4.6 ZSO-IR	100	40.0	-	4.6
M-1.6 ZSO-IR	100	40.0	-	1.6
M-0.60 ZSO-IR	100	40.0	-	0.6

2.6. Dynamic-mechanical analysis

Dynamic mechanical characterization of YZSO-IR and M-YZSO-IR was performed by Rubber Process Analyzer (RPA2000, Alpha Technologies) by applying a shear stress mode. The strain sweep tests were carried out at 70 °C and 10 Hz. Specimens were cut by using a Constant Volume Rubber Sample Cutter (CUTTER 2000, Alpha Technologies); the dimensions were 3.5 cm diameter and ≈ 0.2 cm thick; the weight 4.5 ± 0.3 g. Two measurements were carried out for each sample, and the average value was reported.

3. Results and discussion

3.1. Characterization of ZnO anchored SiO_2 NPs (ZSO-X)

The XRD patterns of ZSO-X (X<14.2) showed amorphous structure whatever the Zn amount, instead ZSO-14.2 and ZSO-50.2 with higher ZnO loading, showed the reflections of the wurtzite phase (JCPDS Card no. 36-1451, Figure S1 in Supporting Information).

TEM and HRTEM images of ZSO-4.0, ZSO-7.7 and ZSO-50.2 are shown in Figure 1.

It can be observed that silica NPs are decorated by very small spherical ZnO NPs, whose size and aggregation depend on the zinc loading, while the average SiO_2 particle size (20-30 nm) remains the same before (Figure S2 in Supporting Information) and after ZnO deposition. In particular, rather

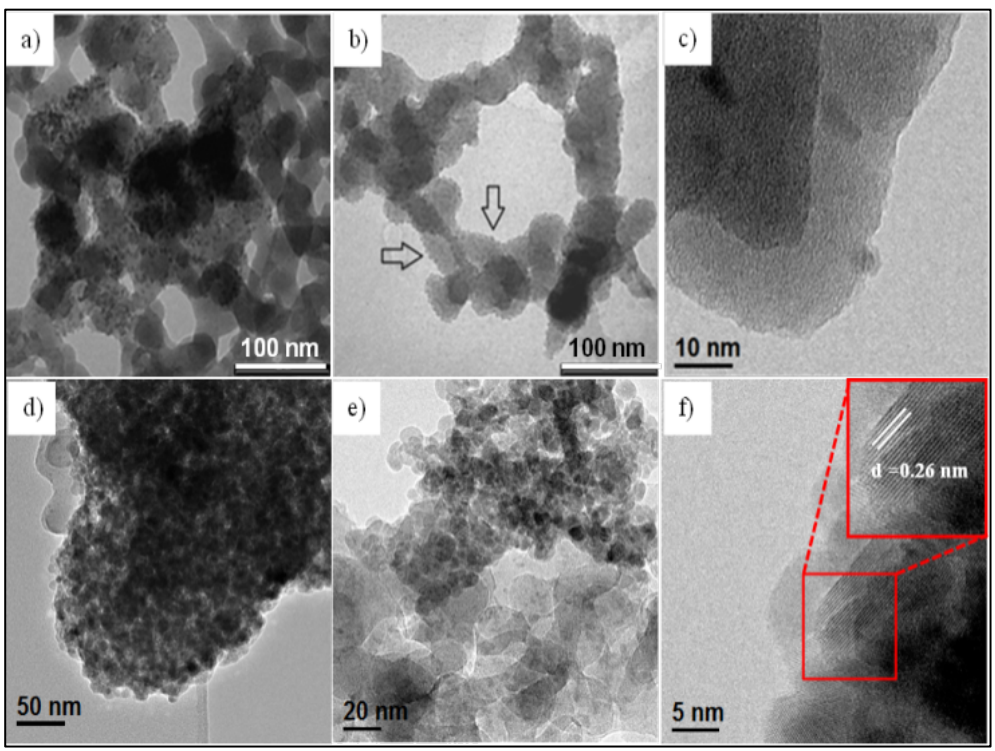

homogeneously dispersed NPs with average diameter 4-6 nm are detectable in ZSO-4.0 and ZSO-7.7 samples (Fig. 1 a, b), while surface aggregates of larger NPs (8-10 nm in diameter) are evident at the highest ZnO concentration (ZSO-50.2, Fig.1 d, e).

Figure 1: TEM and HRTEM images of a) ZSO-4.0; b) and c) ZSO-7.7; d), e) and f) ZSO-50.2.

In agreement with the XRD results, the HRTEM images demonstrate the presence of amorphous ZnO NPs in ZSO composites with lower Zn loading (Fig. 1c), whereas the lattice fringes of the (0002) wurtzite planes are easily identified in the case of ZSO-50.2 (Fig. 1f).

The size of ZnO particles measured by TEM is in accordance with the results obtained by UV-Vis absorption spectra (Fig. 2). In fact the ZSO-50.2 sample, where the largest ZnO NPs are observed, shows a band gap energy (Eg = 3.29 eV) very similar to that of bulk ZnO [28, 29].

Instead, a progressive energy blue-shift takes place for ZSO-7.7 (Eg =3.38 eV) and ZSO-4.0 (Eg = 3.55 eV) [30,31] due to the smaller ZnO NPs dimension (the absorption edge lines in Fig. 2 have been split to draw the tangents and calculate the band gap energy).In order to study the interaction between ZnO particles and SiO_2 and aiming to point out the Si-O-Zn bond formation, solid state ^{29}Si SP MAS, ^{29}Si CP MAS and ^{1}H MAS NMR investigations were performed on ZSO-X samples.

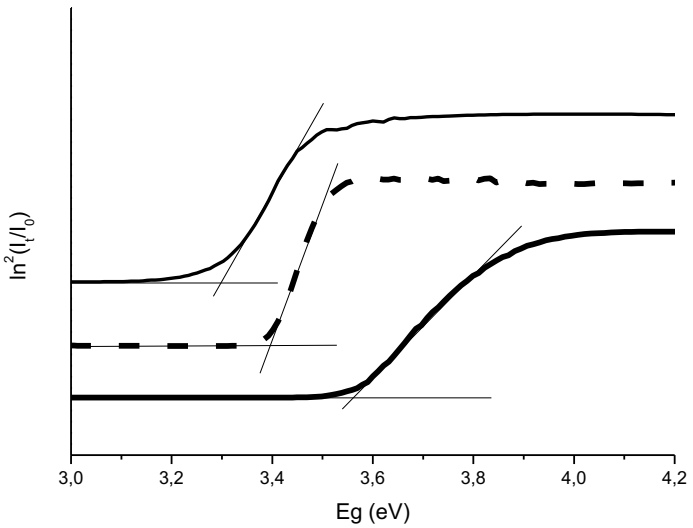

Figure 2: UV-Vis spectra of ZSO-50.2 (——); ZSO-7.7 (— — —); ZSO-4.0 (➡)

The ^{29}Si SP-MAS spectra of ZSO-4.0 and ZSO-7.7 samples show the large signals typical of amorphous structures and are very similar to the spectrum recorded on SiO_2 (Fig. 3). The signals attributed to Q_2, Q_3 and Q_4 resonances present a 2-ppm upfield shift in comparison with the corresponding resonances in

SiO_2, without valuable changes in line-width. The spectrum of ZSO-50.2 with the highest loading of crystalline ZnO (see XRD) shows Q_4 and Q_3 signals and a broad shoulder in the range -70 -100 ppm due to the overlapping of at least four components, suggesting both the presence of pure SiO_2 domains and the formation of Si-O-Zn bonds in different substituted Si units [32, 33].].

The observed shift of Q_n resonances in ZSO-X samples can be explained by the partial substitution of Si-O-Si and Si-OH bonds with Si-O-Zn bonds on the particle surface with consequent changes in the torsion angles T-Ô-T (T stands for a generic cation) [34, 35]. Although Q_n shift values were reported for different zincosilicates [32] there is not a reliable rule for calculating the downfield shift due to Si substitution, as instead is in the well-known case of replacement of OH with Al in SiO_2-Al_2O_3 samples. Thus, although an univocal identification of the Si-O-Zn signals is not possible, the general behavior of ZSO-4.0 and ZSO-7.7 suggests the interaction between ZnO and SiO_2 by means of heterometallic Si-O-Zn bonds.

This conclusion is supported by the results of the quantitative analysis of ^{29}Si SP MAS NMR spectra reported in Table 4. The amount of Q_2 and Q_3 units is higher in the ZSO-X samples than in SiO_2 (according to Q_3/Q_4 and $(Q_2+Q_3)/Q_4$ ratios in Table 4), accounting for the structural changes of the silica surface by interaction with ZnO. Q_2 and Q_3 content slightly decreases moving from the ZSO-4.0 to the ZSO-7.7 sample. This may be associated to an increased aggregation of ZnO particles in ZSO-7.7, which lowers their condensation ability with silica. On the contrary, the strong increase of Q_2 and Q_3 units in ZSO-50.2 is a probable consequence of the different zincosilicate structures, accounting for the resonances between -70 and -110 ppm.

The presence of surface sodium silicate due to the synthesis conditions cannot be excluded (see also XPS analysis), and the related resonances [36] could be hidden under the main peaks of the spectra. However, since the presence of sodium leads to a downfield δ shift of ^{29}Si NMR signals in silica [36-38] the observed upfield shift of Q_n resonances in ZSO-X samples strengthens the hypothesis of Si-O-Zn bond formation. Furthermore, the comparison between the SP MAS spectra of bare SiO_2 before and

after NaOH treatment (not reported) indicates only a slight increase in the number of Q_3 and Q_2 units after the base treatment, without any change in the signal position.

The ^{29}Si CP-MAS NMR spectra of SiO_2 and ZSO-X confirm the SP MAS results (Fig. S3 and Table S1 of Supporting Information). The smaller broadening of ZSO-4.0 and ZSO-7.7 signals compared to SiO_2 resonances can be related to the formation of Si-O-Zn bonds and to the changes in the torsion angles T-Ô-T, as already mentioned above. The semi-quantitative analysis obtained by CP MAS spectra deconvolution (Table S1) shows that the Q_3/Q_4 ratio decreases significantly from pure SiO_2 to ZSO-X samples by increasing the ZnO content. Since the CP-MAS experiment enhances the resonances intensity of Si atoms close to protons, these results suggest a replacement of the surface Si-OH groups with the formation of Si-O-Zn bonds. However, the ^{29}Si CP-MAS spectrum recorded on bare SiO_2 after NaOH treatment displays an increase of the Q_4 units, and consequently both the effect of Si substitution with Zn and the formation of sodium silicate units must be considered.

^{29}Si CP-MAS investigation on ZSO-50.2 revealed the appearance of four new sharp signals (Fig. S3) in the range from -60 to -90 ppm and the increase of Q_3/Q_4 ratio due to the strong large signals observed between -90 and -110 ppm. This confirms a different behavior for this sample compared to composites with lower Zn load. The new signals can account for Si units substituted with a different number of Si-O-Zn bonds, and their sharpness is probably due to the ZnO crystalline features (wurtzite) that induces the formation of symmetrically inequivalent Si-sites [32, 35, 39].

^{1}H MAS NMR spectra (Fig. S4 of Supporting Information) of SiO_2 and ZSO-X samples show peaks due to silanol protons in different hydrogen-bonding environments (Table S2 in Supplementary data) [40, 41]. It is worth of noting that the amount of protons is lower in the ZnO/SiO_2 samples and decreases with the amount of ZnO, thus supporting the silanol replacement with formation of Si-O-Zn bonds.

Table 4. ^{29}Si SP MAS NMR of SiO_2 and ZSO-X samples: relative amount and assignment of the main identified units

			Q_2		Q_3		Q_4		Q_3/Q_4	$(Q_2+Q_3)/Q_4$
	δ (ppm)	**%**	**δ (ppm)**	**%**	**δ (ppm)**	**%**	**δ (ppm)**	**%**		
SiO2	-	-	-91,6	0,6	-100,5	18,2	-110,5	81,3	0,22	0,23
ZSO-4.0	-	-	-92,2	4,1	-102,6	22,8	-112,6	73,2	0,31	0,37
ZSO-7.7	-	-	-92,6	3,8	-102,1	19,5	-112,5	76,6	0,25	0,30
ZSO-50.2	-77,5	4,0	-87,5	12,0	-98,7	27,8	-111,1	56,1	0,50	0,71

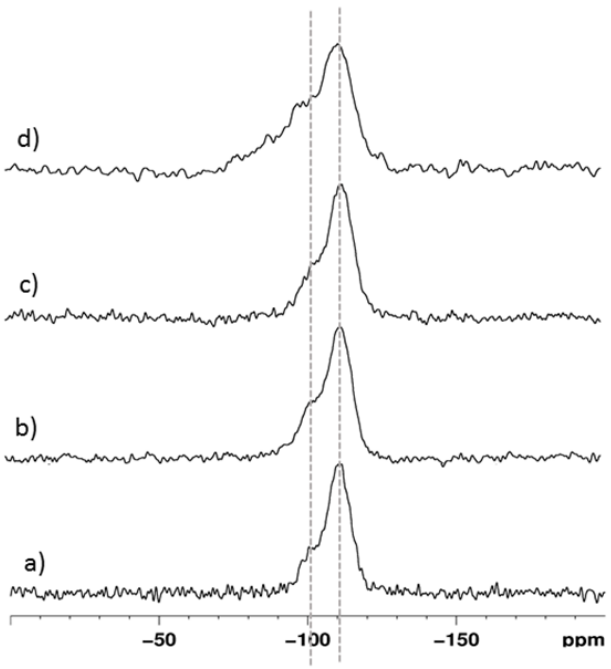

Figure 3: ^{29}Si SP MAS NMR spectra of a) SiO_2; b) ZSO-4.0 ; c) ZSO-7.7 and d) ZSO-50.2

The bond interaction between SiO_2 and ZnO in ZSO-X was also studied by ATR-FTIR spectra of ZSO-X (Figure 4). In this context, the band at 954 cm^{-1} which in bare SiO_2 spectrum was attributed to the –Si-OH [42] stretching vibration (Fig. 4a), in ZSO-4.0 and ZSO-7.7 spectra gradually shifts to higher frequency (~ 963-965 cm^{-1}) and becomes a shoulder (Figure 4 b and c). Referring to the spectra of zincosilicate systems [43] and of ZnO/SiO_2 composites [44, 45] reported in the literature, this change may be attributed to the co-presence of –SiOH and of the symmetric Si-O-Zn stretching modes. This

suggests the formation of covalent bonds between a number of surface silanol groups and the growing ZnO particles in agreement with the NMR results.

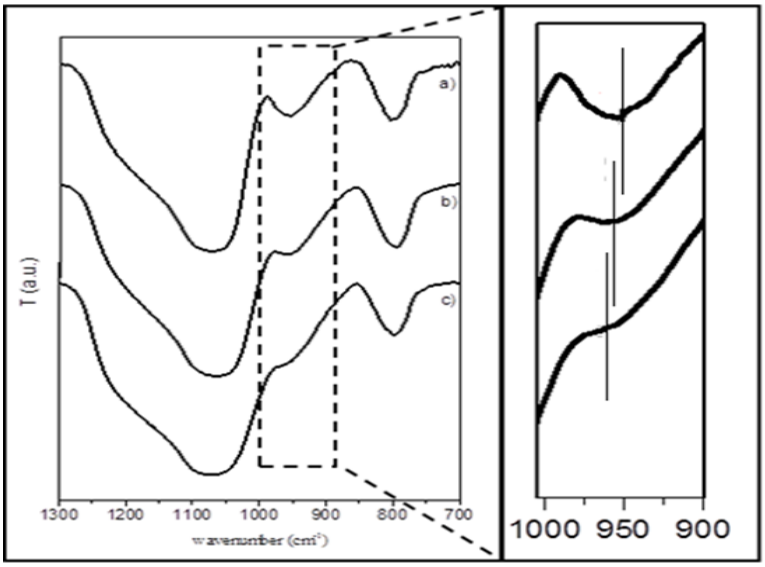

Figure 4: ATR-FTIR spectra of a) SiO_2; b) ZSO-4.0; c) ZSO-7.7. The shift of the –Si-OH stretching vibration is evidenced.

The surface composition of ZSO-X was studied by XPS in comparison with bare SiO_2 treated with NaOH under the same conditions of the ZSO-X synthesis procedure.

The survey spectrum of bare SiO_2 powders treated with NaOH showed the expected silicon and oxygen lines. The energy position of the Si2p peak is at 103.2 eV, whereas the O1s band is centred at 532.5 eV with a small contribution (ca. 10% of the total) at 530.7 eV (Fig. S5 in Supporting Information). This latter component may be likely assigned to the presence of Si-OH and/or Si-O- groups [46] at the surface of silica particles due to the treatment with the sodium hydroxide solution. This also agrees with the observation of the Na1s (BE = 1071.8 eV) line in the spectrum and with NMR results.

In ZSO-4.0 and ZSO-7.7 nanopowders the Si2p and O1s regions showed similar features. Si2p is observed at ~103 eV, whereas the O1s peak displays a slightly asymmetric shape on the low energy side (Fig. 5). Spectral deconvolution of the O1s region reveals the presence of two components. The main peak is centered at 532.5 eV, a binding energy value typical for the silica network [47]; the minor component at lower energy (530.6 – 530.9 eV) is assigned to -OH groups as detected in hydroxide or in

oxo-hydroxo compounds [46]. Similar binding energy values were also attributed to bridging oxygen atoms in Zn-O-Si units at the interface between SiO_2 and ZnO [46].

Remarkably, we did not observe in these samples a clear oxygen component related to a ZnO network, even though the Zn2p line is peaked at a position typical for Zn^{2+} species in an oxide environment ($Zn2p_{3/2}$ = 1021.9 – 1022.0 eV) [46]. These findings support the hypothesis that the wurtzite crystal phase does not form at low ZnO concentrations and suggest that a strong interfacial interaction is established between silica and the amorphous zinc oxo-hydroxo particles thus leading to the formation of bridging Si-O-Zn units. Accordingly, the minor oxygen component represents ca. 10% and 25% of the total oxygen amount in ZSO-4.0 and ZSO-7.7 samples, respectively.

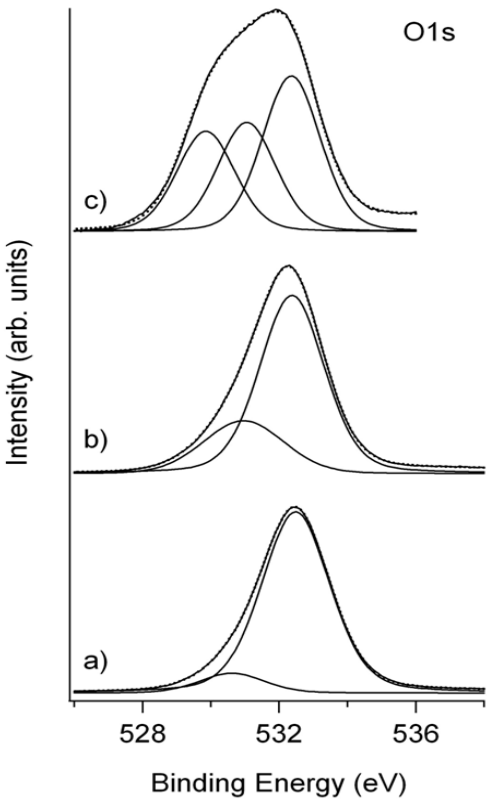

Figure 5: XPS O1s peaks of a) ZSO-4.0; b) ZSO-7.7 and c) ZSO-50.2.

In the high loaded ZSO-X NPs (ZSO-50.2) the O1s peak band shape is broader than previously observed, owing to the presence of oxygen species in different chemical environments. Spectral deconvolution of the peak resulted in three bands centered at 532.3 eV (abundance ~ 40%), 531.1 eV

(abundance ~ 30%) and 529.8 eV (abundance ~ 30%) within experimental uncertainty. Such values account for oxygen atoms in silica, surface hydroxyl and/or oxygen bridging groups, and oxygen in the wurtzite network [48] respectively. The presence of the low energy component is in agreement with the detection of crystalline ZnO in the high loaded samples. Regarding the Zn2p peak, we confirm again the formation of an oxide environment around the Zn^{2+} centers ($Zn2p_{3/2}$ = 1021.1 eV) although we cannot discriminate between the different Zn-OX species (X = H, Zn, Si).

A final observation concerns the purity of the samples. The carbon amount is always on the order of a low % and is mainly due to adventitious contamination (C1s = 284.9 eV). Only in the high ZnO loaded sample we observe a further component at 289.2 eV associated to carbonate species [46]. Hence, it appears that very small residual traces due to the zinc acetate precursor compound are deposited on the surface of the silica particles.

The overall results allow to deeply characterize ZSO-X NPs and to suggest a possible mechanism for the ZnO NPs nucleation on the SiO_2 surface. ZSO-X composites with X<14.2 are constituted by amorphous ZnO spherical NPs chemically interacting with the silica surface. As observed in TEM images, NPs are well dispersed on the filler particles and leave largely exposed silica surface. This suggests that ZnO amorphous NPs are not simply supported, but they grow directly on the silica surface. After the hydrolysis of $Zn(CH_3COO)_2$ in the presence of NaOH, the formation of $Zn(OH)_n^{2-n}$ species occurs. These units then undergo condensation involving SiO_2 hydroxyl surface groups and stabilizing Zn-O-Si covalent bonds. Surface silanol groups may act therefore as nucleation centers for the growth of ZnO NPs chemically linked to silica, as confirmed by the absence of ZnO formation when the reaction is performed without SiO_2.

At higher ZnO loading (ZSO-X with X ≥ 14.2) the surface silanol groups are instead less available, and $Zn(OH)_n^{2-n}$ primarily interact with neighboring Zn-OH surface units forming wurtzite nanocrystals.

ZSO-4.0 samples with the smallest ZnO particle size were selected for the curing test.

3.2. Curing of ZSO-X / IR nanocomposites (YZSO-IR)

The vulcanization curves for YZSO-IR nanocomposites, obtained by measuring the variation of viscosity over the time with the torque requested to keep the rotor at a constant rate, are reported in Figure 6a. Table 3 reports the curing parameters gained from the vulcanization curves of YZSO-IR nanocomposites and also M-YZSO-IR nanocomposites. The minimum torque **ML** is the torque measured at the scorch time $\mathbf{t_{S1}}$, *i.e.* the time during which it is possible to manipulate the rubber composite before curing; the curing time $\mathbf{t_{MH}}$ is the time needed to achieve the complete curing of the composite; the maximum torque **MH** is the torque measured when the reticulation can be considered complete.

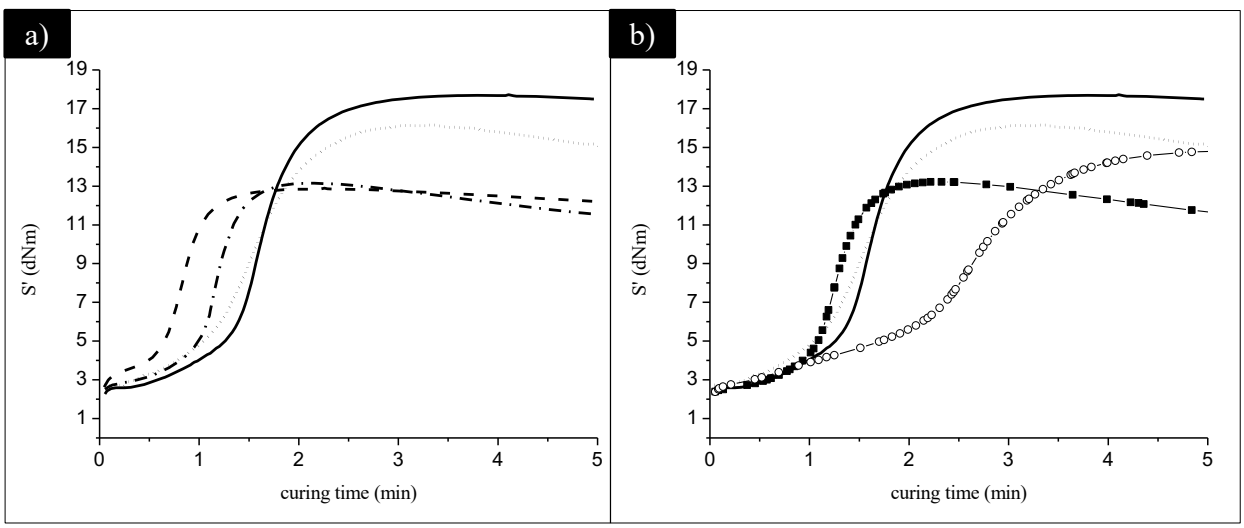

Figure 6. Vulcanization curves of a) 0.05ZSO-IR (– – –); 0.25ZSO-IR (– • – •); 0.6ZSO-IR (••••); 1.60ZSO-IR (——) and b) of 1.60 ZSO-IR (——), M-1.60ZSO-IR(○), and 0.6ZSO-IR (••••), M- 0.60 ZSO- IR(■).

The $\mathbf{t_{MH}}$ and the **MH** values increase with the zinc loading and become highest for the 1.60 ZSO-IR composite (Fig. 6a). It is interesting to note that the 0.05 ZSO-IR sample shows a significant **MH** value, though containing a very small amount of ZnO.

The vulcanization curves were compared with those of M-YZSO-IR composites prepared by using conventional crystalline ZnO as curing activator. Figure 6b shows the comparison between the curves of 1.60 ZSO-IR, 0.60 ZSO- IR and M-1.60ZSO-IR, M- 0.60 ZSO- IR. YZSO-IR composites evidence lower $\mathbf{t_{MH}}$ and higher **MH** than M-YZSO-IR ones though containing the same amount of ZnO. This suggests higher degree of rubber reticulation and more efficient curing mechanism in YZSO-IR composites.

Table 3: Curing parameters of YZSO-IR and M-YZSO-IR samples

Samples	**Min Torque (ML) (kPa)**	**Curing time (t_{MH}) (min)**	**Max Torque (MH) (kPa)**
1.60 ZSO- IR	2.5	1.3	17.7
0.60 ZSO- IR	2.7	1.0	16.1
0.25 ZSO- IR	2.7	0.9	13.1
0.05 ZSO- IR	2.7	0.5	12.8
M- 4.60 ZSO- IR	2.4	2.2	14.8
M- 1.60 ZSO- IR	2.7	1.5	14.9
M- 0.60 ZSO- IR	2.7	1.0	14.4

These outcomes demonstrate the higher curing efficiency in the presence of ZSO-X NPs. This is due to the better dispersion in the matrix, the small dimensions of particles and the weakening of the Zn-O bond energy due to Si-O-Zn interaction. These characteristics should favor an easier release of Zn^{2+} ions compared to crystalline ZnO and the successive formation of the sulfuring zinc-CBS complex along the curing process.

The dynamic-mechanical analyses of cured YZSO-IR and M-YZSO-IR composites were carried out in order to study the effect of the different curing activation on the final properties of the material (Plots of

G' *vs.* strain are shown in Fig. S6 of Supporting Information). The results show that the reinforcing effect of ZSO-X in all YZSO- IR samples is comparable with that in M-YZSO- IR containing the same amount of bare silica (40 phr). This demonstrates that the amorphous ZnO NPs dispersed on the surface of silica does not hinder to form the percolative network responsible for the viscoelastic properties of the composite.

4. Conclusion

In the present study a novel approach is reported, aimed at improving the efficiency of the rubber curing. It employs ZnO NPs anchored to silica filler nanoparticles, which simultaneously behave as curing agent and rubber reinforcing, significantly reducing the amount of the used ZnO activator.

ZSO-X NPs were prepared by hydrolysis and condensation of $Zn(CH_3COO)_2$ in ethanol solution of NaOH in the presence of SiO_2 particles, using very small amounts of the zinc precursor. By this way the hydrolyzed zinc species $Zn(OH)_n^{2-n}$ interact with the silanol groups at the surface of silica particles through Si-O-Zn bonds and induce the growth of ZnO NPs.

In particular, at lower loading of Zn precursor (<14%), ZnO particles have amorphous structure. This property guarantees an easier release of Zn^{2+} ions than in crystalline ZnO NPs, favoring the reaction with stearic acid and the successive formation of the sulfuring zinc complex along the curing process. Moreover, the immobilization of ZnO NPs on the silica surface, due to the covalent Si-O-Zn bond, minimizes the Zn leaching, provides a homogeneous dispersion of zinc and increases the accessibility by curing reactants to Zn^{2+} ions. On the contrary, at higher Zn precursor content the hydrolyzed $Zn(OH)_n^{2-n}$ units further condense giving larger and crystalline ZnO particles anchored to the silica surface, whose activity in curing is lower than that of the amorphous ones.

Amorphous ZnO NPs anchored to silica demonstrated better curing efficiency and improved dynamic mechanical properties in cured silica/rubber nanocomposites, compared to those obtained by using higher amount of microcrystalline ZnO. These results suggest the proposed material could be considered

as a promising system for the improvement of the curing efficacy and for the effective decrease of ZnO utilization in rubber compounding.

Acknowledgements

This work was in the frame of the European COST action MP1202 “Rational design of hybrid organic-inorganic interfaces: the next step towards advanced functional materials”.

Antonio Susanna thanks CORIMAV Foundation for its support within the PCAM European Doctoral Program. Lidia Armelao gratefully acknowledges MIUR for financial support through FIRB Riname RBAP114AMK project.

Appendix A. Supplementary data.

Supplementary data associated with this article can be found, in the online version, at http://dx.doi.org

References

[1] M. Akiba, A.S. Hashim, Vulcanization and crosslinking in elastomers, Prog. Polym. Sci. 22 (1997) 475-521.

[2] N. Rattanasom, A. Poonsuk, T. Makmoon, Effect of curing system on the mechanical properties and heat aging resistance of natural rubber/tire tread reclaimed rubber blends, Polym. Test. 24 (2005) 728-732.

[3] M.R. Krejsa, J. L. Koenig, A Review of Sulfur Crosslinking Foundamental for Accelerated and Unaccelerated Vulcanization, Rubber Chem. Technol. 66 (1992) 376-409.

[4] N.J. Morrison, M. Porter, Temperature Effects on the Stability of Intermediates and Crosslinks in Sulfur Vulcanization, Rubber Chem. Technol. 57 (1984) 63-85.

[5] A.Y. Coran, Cap. 7 in Vulcanization. Encyclopedia of Polymer Science and Engineering 17 (1994) 339-385.

[6] J.A. Brydson, Rubber chemistry, J. Polym. Sci. 20 (1982) 202–203.

[7] V. Duchacek, A. Kuta, Efficiency of Metal Activators of Accelerated Sulfur Vulcanization, J. Appl. Pol. Sci. 47 (1993) 743-748.

[8] Heideman, G. Reduced Zinc Oxide Levels In Sulphur Vulcanisation of Rubber Compounds. Ph.D. Thesis, University of Twente, Enschede - Netherlands 2004.

[9] G. Heideman, R.N. Datta, J.W.M. Noordermeer, Activators in accelerated sulfur vulcanization, Rubber Chem. Technol. 77 (2004) 512-541.

[10] C.G. Moore, M. Porter, Structural Characterization of Natural Rubber Vulcanizates, Rubber Chem. Technol. 36 (1963) 547-557.

[11] G. Heideman, R.N. Datta, J.W.M.Noordermeer, , B. van Baarle, Influence of zinc oxide during different stages of sulfur vulcanization. Elucidated by model compound studies, J. Appl. Polym. Sci 95 (2005) 1388-1404.

[12] A.G. Heath, Water Pollution and Fish Physiology, 1995, CRC Press.

[13] (WHO), W. H. O. Environmental Health Criteria 221 Zinc 2001.

[14] G. Heideman, J.W.M. Noordermeer, R.N. Datta, B. van Baarle, Various Ways to Reduce Zinc Oxide Levels in S-SBR Rubber Compounds, Macromol. Symp. 245-246 (2006) 657-667.

[15] M. Guzmán, N. Agulló, U. Giese, S. Borrós, Exploring tire crumb as activator for sulfur vulcanization, J. Appl. Polym. Sci. 130 (2013) 2809-2820.

[16] P. Bindu, S. Thomas, Viscoelastic Behavior and Reinforcement Mechanism in Rubber Nanocomposites in the Vicinity of Spherical Nanoparticles, J. Phys. Chem. B 117 (2013) 12632-12648.

[17] M. Majid, E.-D. Hassan, A. Davoud, M. Saman, A study on the effect of nano-ZnO on rheological and dynamic mechanical properties of polypropylene: Experiments and models, Composites Part B: Engineering 42 (2011) 2038-2046.

[18] Z. Wang, Y. Lu, J. Liu, Z. Dang, L. Zhang, W. Wang, Preparation of nano-zinc oxide/EPDM composites with both good thermal conductivity and mechanical properties, J. Appl. Polym. Sci. 119 (2011) 1144-1155.

[19] B. Ludi, M. Niederberger, Zinc oxide nanoparticles: chemical mechanisms and classical and non-classical crystallization, Dalton Transactions 42 (2013) 12554-12568.

[20] Y. Chen, M. Kim, G. Lian, M. B. Johnson, X. Peng, Side Reactions in Controlling the Quality, Yield, and Stability of High Quality Colloidal Nanocrystals, J. Am. Chem. Soc. 127 (2005) 127, 13331-13337.

[21] C. Cannas, M. Casu, A. Lai, A. Musinu, G. Piccaluga, XRD, TEM and 29Si MAS NMR study of sol-gel ZnO-SiO2 nanocomposites, J. Mater. Chem. 9 (1999) 1765-1769.

[22] S. Panigrahi, D. Basak, ZnO–SiO_2 core–shell nanorod composite: Microstructure, emission and photoconductivity properties, Chem. Phys. Lett. 511 (2011) 91-96.

[23] N.V. Bondar, M.S. Brodyn, Y.V. Yermolayeva, Emission and percolation of excitons in dense sensembles of quantum dots on spherical surface, Physica E 43 (2011) 1882-1886.

[24] Y.V. Yermolayeva, Y. N. Savin, A.V. Tolmachev, Controlled growth of ZnO nanocrystals on the surface of SiO_2 spheres, Solid State Phenom. 151 (2009) 264-268.

[25] S. Monticone, R. Tufeu, A. V. Kanaev, Complex Nature of the UV and Visible Fluorescience of Colloidal ZnO Nanoparticles, J. Phys. Chem. B 102 (1998) 2854-2862.

[26] D. Briggs, M. Seah, Practical Surface Analysis Wiley, Chichester, 1990.

[27] D.A. Shirley, Phys. Rev. B: Condens. Matter 5 (1972) 4709-4714

[28] L. Irimpan, V.P.N. Nampoori, P. Radhakrishnan, Visible luminescence mechanism in nano ZnO under weak confinement regime, J. Appl. Phys. 104 (2008) 113112-5.

[29] C. Klingshrin, J. Fallert, H. Zhou, J. Sartor, C. Thiele, F. Maier-Flaig, D. Schneider, H. Kalt, 65 years of ZnO research – old and very recent results, Phys. Status Solidi 6 (2010) 1424-1447.

[30] D.W. Bahnemann, C. Kormann, M.R. Hoffmann, Preparation and characterization of quantum size zinc oxide: a detailed spectroscopic study, J. Phys. Chem. 91 (1987) 3789-3798.

[31] H. Yang, Y. Xiao, K. Liu, Q. Feng, Chemical Precipitation Synthesis and Optical Properties of ZnO/SiO2 Nanocomposites, J. Am. Ceram. Soc. 91 (2008) 1591-1596.

[32] C. Cannas, M. Casu, A. Lai, A. Musinu, G. Piccaluga, XRD, TEM and 29Si MAS NMR study of sol-gel ZnO-SiO_2 nanocomposites. J. Mater. Chem. 9, (1999), 1765-1769.

[33] M.A.D. Camblor, E. Mark ^{29}Si MAS NMR Spectroscopy of Tectozincosilicates, J. Phys. Chem. 98 (1994) 13151-13156.

[34] J.K.S. Ramdas, J Klinowki, A simple correlation between isotropic ^{29}Si-NMR chemical shifts and T–O–T angles in zeolite frameworks, Nature 308 (1984) 521-523.

[35] L.B. McCusker, R.W. Grosse-Kunstleve, C. Baerlocher, M. Yoshikawa, M.E. Davis, Synthesis optimization and structure analysis of the zincosilicate molecular sieve VPI-9, Microporous Mater. 6 (1996) 295-309.

[36] L. Martel, S. Cadars, E. Verona, D. Massiot, M. Deschamps, Effects of the orientation of the ^{23}Na–^{29}Si dipolar vector on the dipolar mediated heteronuclear solid state NMR correlation spectrum of crystalline sodium silicates, Solid State Nucl. Magn. Reson. 45-46 (2012) 1–10.

[37] F. Angeli, O. Villain, S. Schuller, S. Ispas, T. Charpentier, Insight into sodium silicate glass structural organization by multinuclear NMR combined with first-principles calculations. Geochim. Cosmochim. Acta 75 (2011) 2453–2469.

[38] K.D. Mackenzie, M.E. Smith, Multinuclear solid-state NMR of inorganic materials. Pergamon materials series 6, Oxford Ed. (2002) cap. 4.

[39] C. Rohrig, I. Dierdorf, H. Gies, X-ray powder diffraction and NMR-spectroscopic investigations on a porous zincosilicate related to the zeolite VPI-7 (VSV), J. Phys. Chem. Solids 56 (1995) 1369-1376.

[40] D.R. Kinney, I.S. Chuang, G.E. Maciel, Water and the Silica Surface As Studied by Variable-Temperature High-Resolution ^{1}H NMR, J. Am. Chem. Soc. 115 (1993) 6786.

[41] S.J. Brus, Solid-State NMR Study of Phase Separation and Order of Water Molecules and Silanol Groups in Polysiloxane Networks. J. Sol-Gel Sci. Technol. 25 (2002) 17–28.

[42] M.G. Fonseca, A.S. Olivera, C. Airoldi, Silylating Agents Grafted onto Silica Derived from Leached Chrysotile, J. Colloid Interface Sci. 240 (2001) 533-538.

[43] A. Roy, S. Polarz, S. Rabe, B. Rellinghaus, H. Zähres, F.E. Kruis, M.Driess, First Preparation of Nanocrystalline Zinc Silicate by Chemical Vapor Synthesis Using an Organometallic Single-Source Precursor, Chem. Eur. J. 10 (2004) 1565-1575.

[44] M. Kotecha, W. Veeman, B. Rohe, M. Tausch, NMR investigations of silane-coated nano-sized ZnO particles. Microp. Mesop. Mater. 95 (2006) 66-75.

[45] X. Collard, M. El Hajj, B. L. Su, C. Aprile, Synthesis of novel mesoporous ZnO/SiO_2 composites for the photodegradation of organic dyes, Microporous Mesoporous Mater. 184 (2014) 90-96.

[46] J.F. Moulder, W.F. Stickle, P.E. Sobol, K.D. Bomben, Handbook of X-ray Photoelectron Spectroscopy, Ed. G. Chastain, Perkin Elmer Corporation, Eden Prairie (Minnesota) 1992

[47] L. Armelao, P. Colombo, G. Granozzi, M. Guglielmi, SiO_2-TiO_2 sol-gel coating: a surface study by X-ray photoelectron spectroscopy, J. Non-Cryst. Solids 139 (1992) 198- 204

[48] L. Armelao, G. Bottaro, M. Pascolini, M. Sessolo, E. Tondello, M. Bettinelli, A. Speghini, Structure-luminescence correlations in europium-doped sol-gel ZnO nanopowders, *J. Phys. Chem. C,* 112 (2008) 4049-4054.